photonics

MDPI

Article

Generation and Detection of Optical Vortices with Multiple Cascaded Spiral Phase Plates

Ziheng Zhou [1], Peng Li [1,2,*], Jingbo Ma [1], Shirui Zhang [1] and Yuzong Gu [1,2]

[1] Research Center for Physics of 2D Opto-Electronic Materials and Devices, School of Physics and Electronics, Henan University, Kaifeng 475004, China; zzh12821@163.com (Z.Z.); 17352576816@sina.cn (J.M.); zhangsr925@163.com (S.Z.); yzgu@vip.henu.edu.cn (Y.G.)

[2] International Joint Research Laboratory of New Energy Materials and Devices of Henan Province, Kaifeng 475004, China

* Correspondence: lilipengpeng@vip.henu.edu.cn

Abstract: Spiral phase plate (SPP) is the widely used method in the generation of vortex beam (VB) with fixed topological charges (TCs) for specific wavelength. Although VB with large TCs can be directly generated by using the SPP with high vortex order. The fabrication of high-quality SPPs with high vortex orders usually requires complex manufacturing process and high machining accuracy. An alternative method to generate VBs with large TCs is cascaded multiple SPPs with low order. In this study, we numerically calculate the transmitted light field of cascaded multiple SPPs according to the Huygens–Fresnel diffraction integral, and perform the experimental verifications. Based on cascading 6 SPPs (3 SPPs with TCs of 2, and 3 SPPs with TCs 4, respectively), an VB with TCs as high as 18 is generated. Furthermore, The TCs of the generated VB are detected by coaxial and off-axis interfering with fundamental Gaussian beam or its conjugate beam, respectively. The generated fork and spiral patterns allow us to distinguish the value and sign of TCs carried by the VB. The experimental results coincide well with the theoretical simulations. The fork pattern shows better resolution than the spiral one, and the petal pattern with small spiral allows us to distinguish large TCs with a higher resolution.

Keywords: optical vortex; spiral phase plates; topological charge; cascaded configuration; interference discrimination method

Citation: Zhou, Z.; Li, P.; Ma, J.; Zhang, S.; Gu, Y. Generation and Detection of Optical Vortices with Multiple Cascaded Spiral Phase Plates. *Photonics* **2022**, *9*, 354. https://doi.org/10.3390/photonics9050354

Received: 23 April 2022
Accepted: 17 May 2022
Published: 18 May 2022

1. Introduction

Vortex beams (VBs) with large topological charge (TC) and large area of dark core have a great application prospect in fields such as optical microscopy [1,2], hyper-entanglement [3,4], high-sensitivity spatial measurement [5,6], high-capacity optical communication [7], and optical manipulation of object with large volume [8]. Laguerre–Gaussian modes (LG_{pl}, p, and l are radial and azimuthal indices) are representative and widely studied VBs containing $\exp(il\varphi)$ term. Here $c\varphi$ is the azimuthal angle and l is called the TCs of the VB. Usually, the VB of charge l carries an orbital angular momentum (OAM) of $l\hbar$ per photon [9,10]. The beam pattern of VB with LG_{0l} mode shows a doughnut shaped structure. So far as we know, various methods based on spatial light modulators, digital micromirror devices, spiral phase plates (SPPs), photon sieves, metasurfaces, etc. have been proposed to generate VBs in the extra-cavity laser scheme [11–15]. With respect to the other techniques, SPPs provide a stable, efficient, and compact method for VB generation from common laser beams. Particularly, SPPs made of silicon can operate under high laser power.

SPP, as one of the most used refractive optical elements, is a dielectric plate with spiral thickness profile, where the optical height is proportional to the azimuthal angle φ. VBs with spectrum ranging from microwave to X-ray are obtained through different kinds of SPPs [16–38]. Early in 1992, S. N. Khonina, et al. reported the creation of the phase rotator filter (an optical element whose complex transmittance function $\exp(i\varphi)$ depends on the azimuth angle φ, it is called SPP later) at 633 nm by photolithography techniques for the first time [16]. In 1994, M. W. Beijersbergen, et al. demonstrated that a SPP at 633 nm can convert a TEM_{00} laser beam into a helical-wavefront beam with a phase singularity at its axis [17]. In 1996, G. A. Turnbull, et al. used a SPP at millimeter-wave frequencies to transform a free-space, fundamental Hermite–Gaussian mode in a LG mode with an azimuthal phase component [18]. In 2002, G. Machavariani, et al. realized efficiently converting a Gaussian beam into a helical LG beam with efficiency as high as 98%; they use a pair of axicons to produce a shifted Gaussian intensity distribution that is then passed through a SPP at 1064 nm [19]. A. G. Peele, et al. reported an experimental observation of an optical vortex in a field consisting of 9-keV X-ray photons created by the SPP [20]. In 2004, K. Sueda, et al. demonstrated the generation of a LG beam with a doughnut-shaped intensity pattern by applying a multilevel SPP at 780 nm [21]. At the same year, T. Watanabe, et al. generated the first-order of Bessel beam by a SPP with 8 divided etching areas [22]. C. Rotschild, et al. constructed a spiral phase retarder with the use of a deformed cracked plexiglass plate [23]. X. C. Yuan and coworkers reported on the performance of four kinds of SPPs (an irregular-shaped SPP, a micron-sized SPP, a solitary kinoform-type SPP, and a radially modulated SPP, respectively) fabricated by electron-beam lithography [24–27]. Q. Wang, et al. generated doughnut-shaped beams with charges from 1 to 6 at wavelength of 633 nm by using liquid-crystal SPPs [28,29]. S. S. R. Oemrawsingh, et al. fabricated high-quality, half-integral SPPs, and smooth SPPs based on molding technique for generating optical vortices at visible and near-infrared wavelengths with TCs of 3.5 and 5 respectively [30,31]. In 2014, G. Ruffato, et al. designed and fabricated SPPs at 633 nm for the generation of LG beam with non-null radial index by electron beam lithography on polymethylmethacrylate over glass substrates [32]. P. Schemmel, et al. presented a modular SPP to generate millimeter wavelength beam with an azimuthal mode number of $l = \pm 10$ [33]. In 2015, L. F. Shi, et al. presented the fabrication of SPPs at 532 nm with continuous surface by using an economical method, and generated VB with TCs as high as 20 by the fabricated SPP [34]. M. Massari, et al. realized the generation of high-order LG beams with different values of TC and radial index by the use of high-quality single- and multi-step SPPs, which is fabricated by electron beam lithography [35]. W. Harm, et al. reported on the experimental demonstration of the conversion of a TEM_{00} beam into approximated LG beams of variable TCs from 1 to 10 for a fixed wavelength 532 nm by using Moiré diffractive SPPs [36]. In 2019, a flat SPP was introduced by W. B. Wu, et al., the height of which remains unchanged, whereas the refractive index increases with the azimuthal angle [37]. In 2020, D. Isakov, et al. generated electromagnetic waves with OAM mode number $l = \pm 1$ in the 12–18 GHz frequency range by using the dielectric SPPs, which were additively manufactured using material extrusion and polyjet fabrication methods [38]. A specific SPP is rather sensitive to the wavelength of the laser, and only suitable for the generation of VB with specific TC. Due to the demanding of machining accuracy, the fabrication of high quality SPPs with large TCs is usually complicated and expensive [34]. VBs with large TCs can also be generated by cascading multiple low-order SPPs. In 2004, Q. Wang, et al. found that stacking liquid-crystal SPPs yielded doughnut beams with charge numbers up to 8 with high efficiency and flexibility [29]. In 2016, Y. Wei, et al. presented the research on the generation of VB by superposition of two SPPs [39]. In 2018, C. Wang, et al. reported on the addition of TCs by cascading two SPPs, doubling of TCs by double-pass configuration, and quadrupling TCs by passing SPP with four times, respectively [40–42]. They found that the cascaded SPPs scheme has the advantage of the reduced reduction of the relative intensity, the degree of radius divergence, and possibility of decomposition of VB because of the instability of high order over the single SPP scheme [40]. The cascaded SPPs scheme is entirely better than single SPP in generating VB. However, only the cascaded scheme with two SPPs had been studied, and there are few reports on the performance of VB generated by cascading multiple SPPs (>2).

Precisely measuring TCs is important due to the OAM per photon relating to the TCs of VB. Various methods, including interference methods [43–51], diffraction methods [52–54], and mode transformation methods [55–57], etc., have been used to determine the TCs carried by the VB. Methods based on interference of two beams are widely used to measure the TCs of VB. Usually, one VB is arranged to interfering with a fundamental Gaussian beam or its conjugate one. Different kinds of patterns, including fork pattern [43–45], spiral pattern [46–48], and petal pattern [49–51], are obtained by carefully choosing the oblique angle and wavefront curvature radii of two interference beams. The comparison of these patterns for VBs with larger TCs are seldomly studied.

In this paper, VBs with large TCs are generated by cascading multiple SPPs, both experimentally and in theory. The interference discrimination methods for TCs are compared under different TCs. Section 2 is the mathematical form of VBs after passing through multiple SPPs. Section 3 is devoted to the description of the experimental setup. Experimental results and simulations, including beam pattern of VBs for cascading different SPPs, the interference patterns between VB and its conjugate one (or the fundamental Gaussian beam), are discussed in Section 4. Finally, the conclusion is presented in Section 5. This work provides the effective methods for generating VBs with large TCs by cascaded multiple (>2) low-order SPPs and discriminating TCs.

2. Theoretical Analysis

In this part, we demonstrate the transformations of the fundamental Gaussian beam after passing through multiple SPPs (n SPPs with vortex orders of $l_1, l_2, \ldots, l_n$, respectively) in the cascaded configuration, as shown in Figure 1. A reverse transmission of the SPP adds sign-reversed TCs compared with a transmission of the forward direction. Here we assume all SPPs are placed with the same side facing the light beam, such that the generated VB bears TCs of $\pm\sum_{i=1}^{n} l_i$. Finally, the VB illuminates the camera for observation after passing propagation distance z_n.

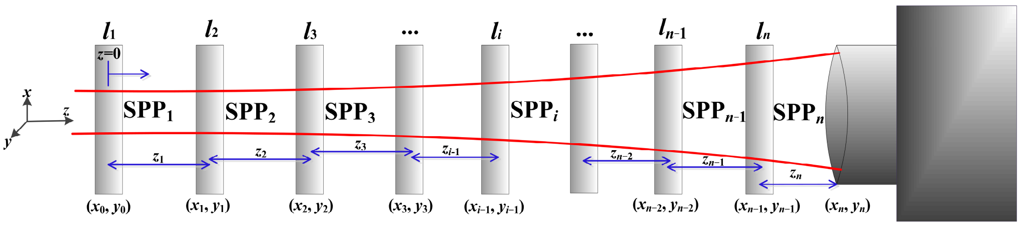

Figure 1. Schematic diagram showing the multiple cascaded SPPs. SPP$_n$ is located at x_{n-1}–y_{n-1} plane. The distance between SPP$_{n-1}$ and SPP$_n$ is z_{n-1}, and the distance between SPP$_n$ and the camera is z_n.

We assume SPP$_1$ is located at the waist position of the fundamental Gaussian beam. VB of TCs $\pm\, l_1$ are generated by modulating the fundamental Gaussian beam with SPP$_1$ (order l_1) with a transmission function $\exp[i|l_1|\arg(x_0 \pm iy_0)]$, where "±" denotes the sign of TCs. Detail calculations using Fresnel diffraction theory or Collins–Huygens illustrate that the amplitude of the generated doughnut beam by the SPP is proportional to the difference of two first kind Bessel functions with numbers $(l_1 + 1)/2$ and $(l_1 - 1)/2$ orders, and the calculation processes are very complicated [58,59]. Considering the LG$_{0l}$ beam dominates in the generated doughnut beam [17], we take the approximation that the doughnut beam is LG$_{0l}$ mode for simplicity. The transmission function of SPP$_1$ can be expressed as $(x_0 \pm iy_0)^{|l_1|}$.

At the x_0–y_0 (z = 0) plane, the field distribution of VB can be expressed as

$$E_0(x_0, y_0, 0) \propto (x_0 \pm iy_0)^{|l_1|} \exp[-(x_0^2 + y_0^2)/w_0^2] \tag{1}$$

where the waist w_0 is the radius for which the Gaussian term falls to 1/e of its on-axis value.

According to the Huygens–Fresnel integral, the field distribution of VB in x–y plane at a distance z from SPP$_1$ can be expressed as [40–42]

$$E(x, y, z) = \frac{ik\exp(-ikz)}{2\pi z}\int\int dx_0 dy_0 \exp[-ik\frac{(x - x_0)^2 + (y - y_0)^2}{2z}]E_0(x_0, y_0, 0). \tag{2}$$

where $k = 2\pi/\lambda$ is the wave number. Substituting Equation (1) into Equation (2), and using the binomial theorem:

$$(x_0 + iy_0)^m = \sum_{l=0}^{m} \frac{m! i^l}{l!(m-l)!} {x_0}^{m-l} {y_0}^l. \tag{3}$$

and integral formula [60]

$$\int_{-\infty}^{\infty} x^n \exp\left(-bx^2 + 2cx\right) dx = n! \sqrt{\frac{\pi}{b}} \left(\frac{c}{b}\right)^n \exp\left(\frac{c^2}{b}\right) \sum_{u=0}^{n/2} \frac{1}{u!(n-2u)!} \left(\frac{b}{4l^2}\right)^u. \tag{4}$$

The field distribution in Equation (2) takes the form

$$E(x,y,z) \propto \left(\frac{ik}{2\gamma_1 z}\right)^{|l_1|+1} \exp\left(-\frac{x^2+y^2}{w_1^2}\right) (x \pm iy)^{|l_1|} e^{-ikz}. \tag{5}$$

Here $\gamma_1 = 1/w_0^2 + ik/(2z)$, and $1/w_1^2 = k^2/(4\gamma_1 z^2) + ik/(2z)$.The intensity of such VB can be expressed as:

$$I = 2n_i c\varepsilon_0 |E(x,y,z)|^2. \tag{6}$$

where n_i is the refractive index of the transmission medium, ε_0 is the permittivity of vacuum, and c is the speed of light in vacuum. In general, the intensity expression of the VB after SPP_1 has the following form:

$$I \propto \exp(-2\frac{x^2+y^2}{w'^2_1})(x^2+y^2)^{|l_1|}. \tag{7}$$

Here ${w_1}'$ is the equivalent beam radius of the fundamental mode corresponding to the VB, and $w'^2_1 = w_0^2(1+z^2/z_R^2)$. $z_R = \pi w_0^2/\lambda$ is the Rayleigh length.

Consider the SPP_2 located at (x_1, y_1, z_1). The field expression of VB propagating in a distance z_1 in x_1–y_1 plane after SPP_1 is denoted by

$$E_1(x_1,y_1,z_1) \propto \left(\frac{ik}{2\gamma_1 z_1}\right)^{|l_1|+1} \exp\left(-\frac{{x_1}^2+{y_1}^2}{{w_1}^2}\right) (x_1 \pm iy_1)^{|l_1|} e^{-ikz_1}, \tag{8}$$

and the transmission function of SPP_2 is $(x_1 \pm iy_1)^{|l_2|}$. Using the similar process, the field expression of VB propagating a distance z_2 in x_2–y_2 plane after SPP_2 is denoted by

$$\begin{aligned} E_2(x_2,y_2,z_2) &= \iint \tfrac{ike^{-ikz_2}}{2\pi z_2} dx_1 dy_1 \exp\left[-ik\tfrac{(x_2-x_1)^2+(y_2-y_1)^2}{2z_2}\right] E_1(x_1,y_1,z_1)(x_1 \pm iy_1)^{|l_2|} \\ &\propto \left(\tfrac{ik}{2\gamma_1 z_1}\right)^{|l_1|+1} \left(\tfrac{ik}{2\gamma_2 z_2}\right)^{|l_1|+|l_2|+1} \exp\left(-\tfrac{{x_2}^2+{y_2}^2}{{w_2}^2}\right)(x_2 \pm iy_2)^{|l_1|+|l_2|} \exp\left[-ik(z_1+z_2)\right]. \end{aligned} \tag{9}$$

where $\gamma_2 = 1/{w_1}^2 + ik/(2z_2)$, $1/{w_2}^2 = k^2/(4\gamma_2 {z_2}^2) + ik/(2z_2)$. The intensity expression of the VB after cascaded of SPP_1 and SPP_2 has the following form:

$$I \propto \exp(-2\frac{x^2+y^2}{w'^2_2})(x^2+y^2)^{|l_1|+|l_2|}. \tag{10}$$

Here ${w_2}'$ is the equivalent beam radius of the fundamental mode corresponding to the VB, and $w'^2_2 = w_0^2\left[1+(z_1+z_2)^2/z_R^2\right]$.

Similarly, the field expression of VB propagating in a distance z_n in a x_n–y_n plane after SPP_n is denoted by

$$E_n(x_n,y_n,z_n) \propto \prod_{j=1}^{n} \left(\frac{ik}{2\gamma_j z_j}\right)^{1+\sum\limits_{m=1}^{j}|l_m|} \exp\left(-\frac{{x_n}^2+{y_n}^2}{{w_n}^2}\right)(x_n \pm iy_n)^{\sum\limits_{m=1}^{n}|l_m|} \exp\left[-ik\left(\sum_{m=1}^{n} z_m\right)\right]. \tag{11}$$

where $\gamma_j = \frac{1}{w_{j-1}{}^2} + \frac{ik}{2z_j}$ $(j \geq 1)$ and $\frac{1}{w_j{}^2} = \frac{k^2}{4\gamma_j z_j{}^2} + \frac{ik}{2z_j}$ $(j \geq 1)$. As a whole, the process of n transformations makes a combination of TCs with $\pm\sum_{i=1}^{n} l_i$. The intensity expression of the VB after cascading multiple SPPs has the following form:

$$I \propto \exp(-2\frac{x^2+y^2}{w'^2_{\mathrm{n}}})(x^2+y^2)^{\sum_{i=1}^{n}|l_i|}. \tag{12}$$

Here $w_{\mathrm{n}}{}'$ is the equivalent beam radius of the fundamental mode corresponding to the VB, and $w'^2_{\mathrm{n}} = w_0^2[1+(\sum\limits_{j=1}^{n} z_j)^2/z_R^2]$. $w_{\mathrm{n}}{}'$ increases with the distance z_j. The corresponding VB possesses the radius of $w_{0l} = w'_{\mathrm{n}}\sqrt{1+\sum\limits_{j=1}^{\mathrm{n}}|l_j|}$, and it enlarges quickly with increasing TCs.

3. Experimental Setup

The schematic diagram of the experimental setup is shown in Figure 2. A TEM_{00} green laser delivers a collimated Gaussian beam at 532 nm. The polarizer is used to ensure the laser used is linearly polarized light. The beam is diffracted by a circle pinhole with a diameter of 100 µm. After that, the laser beam is truncated by a circular diaphragm that only allows the Airy spot passing through. Then the beam is collimated with a lens of focus length 200 mm. The SPPs designed at 1064 nm with vortex orders l = 1, and 2 [34,43,47] are used here. The corresponding vortex orders of SPPs for 532 nm are, approximately, 2 and 4, respectively. All SPPs are mounted on the two-dimensional translation frames. Remarkably, when a new SPP is inserted on the optical path, its position should be carefully adjusted, so that the new generated dark core coincides with the dark core of the original VB. The intensity pattern is recorded by a CMOS camera. The TCs of VB is detected by the interference discrimination method, which was described in our previous work [43,47] in detail and not shown here.

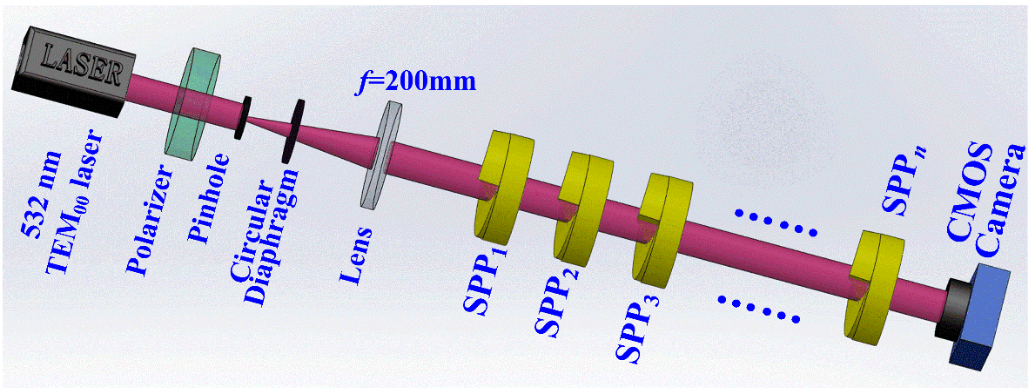

Figure 2. Schematic of the experimental setup.

4. Results and Discussion

4.1. High Order VB Generated by Multiple Cascaded SPPs

The combination of 3 pieces of SPPs with vortex order 2 and 3 pieces of SPPs with vortex order 4 allows the generation of VB with TCs up to 18 during our experiments. During the simulations, the beam radius w is chosen to be 1.3 mm, and the distance z_i between two adjacent SPPs (SPP and camera) is chosen to be 50 mm (200 mm), respectively. Each simulation is displayed in a two-dimensional frame with size of 11 mm × 11 mm. Intensity distributions and phase maps of VB with TCs from 2 to 18 in steps of 2 are depicted in Figure 3. The detailed arrangements of cascaded SPPs are introduced as follows. With a single SPP of vortex order 2, VB with TCs 2 is generated, as shown in column 1 of Figure 3. When two SPPs are cascaded, VBs with TCs of 2 + 2 and 4 + 4 are generated, respectively (as shown in columns 2 and 4 of Figure 3). When three SPPs are cascaded, VBs with TCs of 2 + 2 + 2 and 4 + 4 + 4 are generated, respectively (as shown in columns 3 and 6 of Figure 3). For four cascaded SPPs, VB with TCs of 2 + 2 + 2 + 4 is generated (as shown in column 5 of Figure 3). For five cascaded SPPs, VBs with TCs of 2 + 2 + 2 + 4 + 4 and 2 + 2 + 4 + 4 + 4 are generated (as shown in columns 7 and 8 of Figure 3). For all six cascaded SPPs, VB with TCs of 2 + 2 + 2 + 4 + 4 + 4 is generated (as shown in column 9 of Figure 3). Rows (a) and (b) of Figure 3 show the intensity patterns of the ring VBs bearing different TCs in experiment and theoretically. For the experimental patterns, since not all the VB patterns are located at the center of camera, and the positions of camera are changed for detecting the whole pattern of VB with large TCs, we only cut out the image of the VB, and we cannot compare the beam size of VBs with different TCs. Figure 3a1–a9 demonstrates that the central dark area is broader with the increase of the magnitude of TCs. Figure 3b1–b9 illustrates that with increasing the magnitude of TCs, the VB spot enlarges and the central dark area is broader. Experimental results are consistent with the simulation ones, except outer concentric rings. These outer rings in the surroundings of doughnut beam seen in experiment are due to the presence of higher-order modes whose origins lie in the purity of the mode conversion by SPPs. However, the annular VB generated in experiment is not uniform. This may be due to two category factors. On the one hand, the real vortex orders of our SPPs at 532 nm are 2.049 and 4.098 for the SPPs with nominal vortex orders of 1 and 2 at 1064 nm, respectively. This is verified by the tail [30] at the upper right corner of Figure 3a1. On the other hand, the pinhole is not round enough, the machining accuracy of the SPP is not high enough, and the beam does not pass through the center of every SPP. The quality of VB generated in experiment becomes deterioration, and high order modes LG_{pl} ($p > 0$) gradually become obvious with increasing the number of cascaded SPPs, due to the difficulty in aligning all the SPPs' centers on the same axis. Row (c) of Figure 3 depicts the numerically calculated phase map of the VB. The phase map can be divided into l identical parts, and rotates counter-clockwise. This is because the sign of TC in our study is positive.

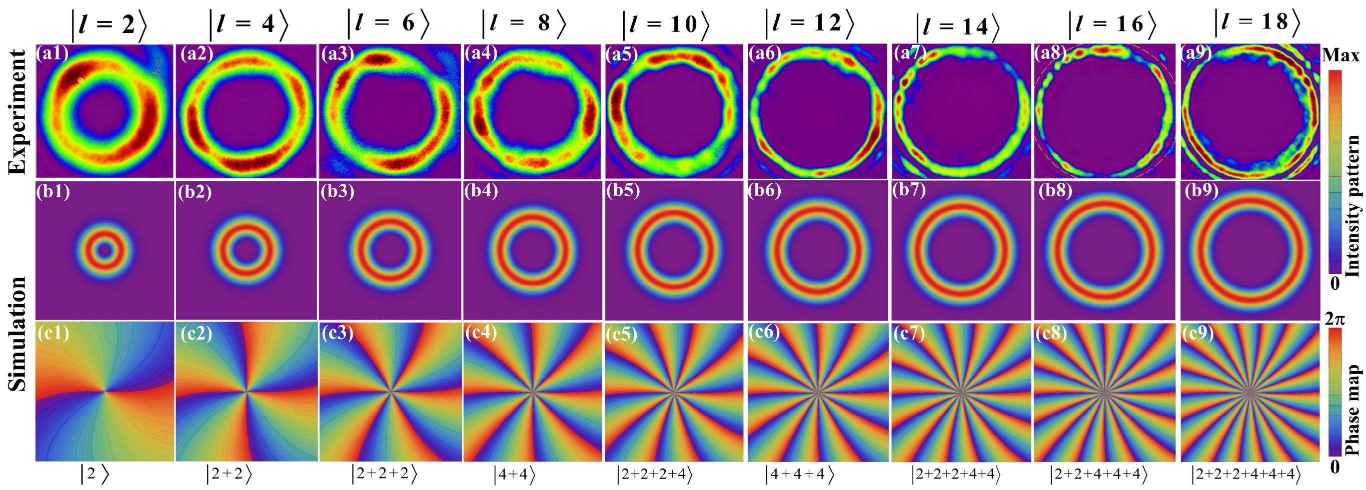

Figure 3. The VB with TCs from 2 to 18 based on multiple cascaded SPPs. (**a1**–**a9**) the experimental intensity pattern; (**b1**–**b9**) the simulated intensity pattern; (**c1**–**c9**) the simulated phase map.

4.2. Interference between a VB and a TEM_{00} Gaussian Beam (or Its Conjugate One)

To discriminate the TCs of VB, VB is usually used to interfere with a Gaussian beam (or its conjugate one). According to the oblique angle between two interference beams, there exist off-axis interference and coaxial interference. The later one can be further divided according to the relation of the wavefront curvature radii of two interference beams.

When there exists an oblique angle between two interference beams, fork-shaped pattern will form [43–45]. TCs of VB is determined by both the fork direction and the oblique angle θ. The fork number is equal to the module of TCs difference between two vortex beams $l_1 - l_2$, and the fork direction is determined by both the sign of oblique angle θ and TCs difference $l_1 - l_2$, upward for the same sign and downward for the opposite sign. Figure 4 shows the off-axis interference patterns between a VB with TCs from 2 to 8 and a TEM_{00} Gaussian beam (its conjugate one). During the experiment, the oblique angle θ is slightly adjusted to improve the resolution of the fork fringes for higher TCs. This is the reason that the fringes are denser for higher TCs. As shown in Row (a) of Figure 4, the fork direction is upward, and the fork number, which is the module of fringe difference between both ends of the fork, is just the TCs value l of VB. This is because the oblique angle θ is positive, $l_1 = l$, and $l_2 = 0$, thus resulting in $l_1 - l_2 = l$ during the experiment. Row (b) of Figure 4 shows the off-axis interference between a VB and its conjugate one. Here θ is still positive, $l_1 = l$, $l_2 = -l$, and $l_1 - l_2 = 2l$. The fork direction is still upward, and the fork number is $2l$. However, the fork number is hard to distinguish for large value l. This is because the larger value of $2l$ needs more density fringes to count.

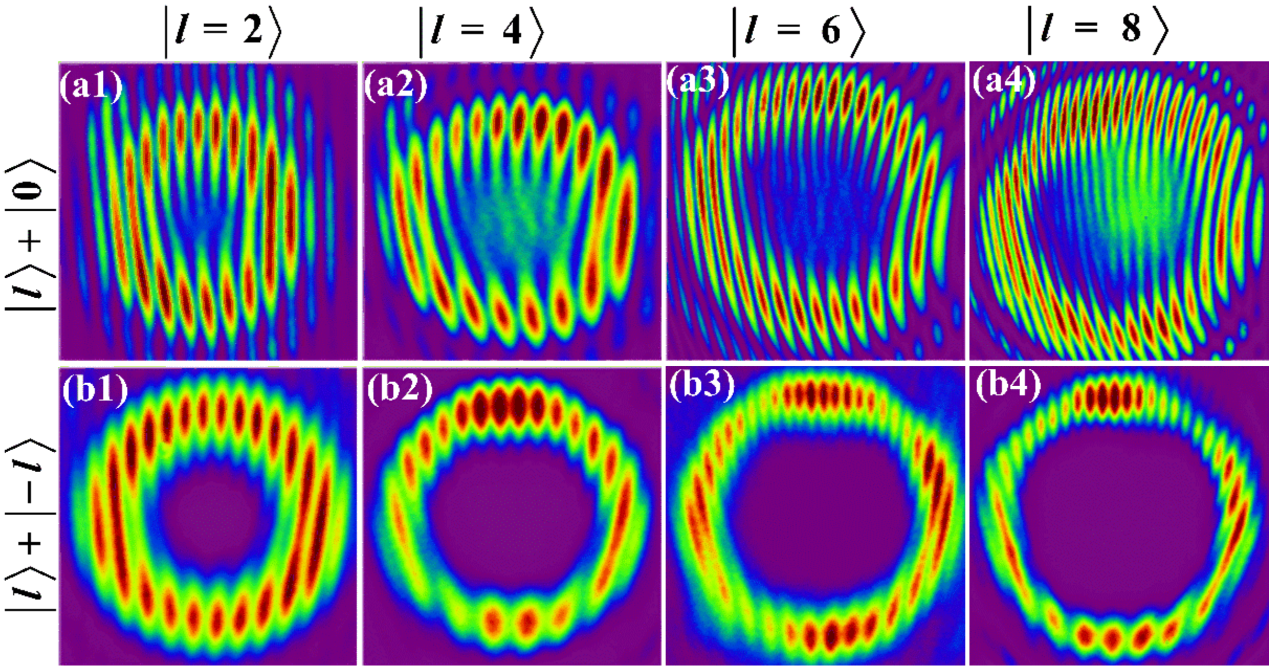

Figure 4. Off-axis interference patterns for VBs with TCs from 2 to 8. Images (**a1**–**a4**) are interference patterns between VB and a TEM_{00} Gaussian beam; Images (**b1**–**b4**) are interference patterns between VB and its conjugate one.

We take the off-axis interference patterns between a VB with TCs 14 and a TEM_{00} Gaussian beam (its conjugate one) (shown in Figure 5) as an example for detailed introduction. For the off-axis interference pattern, fork point is the location of the vortex (singularity). As shown in Figure 5a, there exist 14 fork points, and there is a single vortex with TC + 1 at each fork point. It demonstrates that the VB contains 14 single vortices with TC + 1, rather than one vortex with TCs of 14. This is mainly due to two reasons. On the one hand, not all SPPs' centers coincide well with the beam center in the real experiment. On the other hand, the presence of a coherent background changes the location of a vortex which was initially localized at the center of the VB [26,61,62]. As shown in Figure 5b, considering the fringes two black dash lines, the fringes numbers are 44 on the upper side and 16 on the lower side, respectively. The difference of fringes numbers on both side is 28, which is just $2l$. We also notice that the poor beam spot for large TCs leads to nonuniform of the interference fringes' brightness, thus resulting in difficulty to count the fringes clearly.

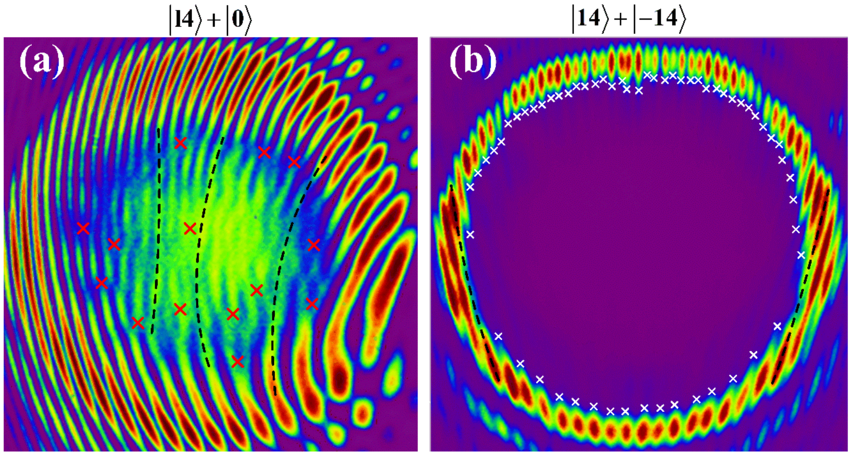

Figure 5. Off-axis interference patterns for VB with TCs 14. Image (**a**) is interference pattern between VB with TC of 14 and a TEM_{00} Gaussian beam; Image (**b**) is interference pattern between VB with TC of 14 and its conjugate one. Black dotted lines are guideline for the interference fringes. The red crosses are used to denote the forks' locations in image (**a**), and the white crosses denote the fringes between two black dotted guideline of fringes image (**b**).

When two vortex beams with different wavefront curvature radii interfere coaxially, spiral pattern will form. For two VBs bearing TCs of l_1 and l_2 (simply denoted by l_1 and l_2), the number of spiral lobes depend on the absolute value of TCs' difference $l_1 - l_2$, and the twist direction depends on the sign of TCs' difference $l_1 - l_2$ and difference of reciprocals for wavefront curvature radii $(1/R_{l_1} - 1/R_{l_2})$, clockwise for the same sign, and counter-clockwise for opposite signs [46–48]. During our experiments, the fundamental Gaussian beam and VB with TCs $-l$ are focused. In order to make the spiral pattern under large TCs clear, the lens with longer focal length is used to focus the beam. Figure 6 depicts images of coaxial interference patterns between the VB with TCs from 2 to 8 and the divergent beam. As shown in Row (a) of Figure 6, the twist direction is counter-clockwise, and the number of helixes is just the TCs l of VB. This is because $l_1 - l_2 = l - 0 = l$, and $1/R_{l_1} < 1/R_{l_2}$. Row (b) of Figure 6 shows the coaxial interference between a VB and its conjugate one. The relation $1/R_{l_1} < 1/R_{l_2}$ still holds. For the case, $l_1 = l$, $l_2 = -l$, and $l_1 - l_2 = 2l$. The twist direction is still counter-clockwise, and the number of helixes is $2l$. Both two kinds of helixes are hard to count for large l.

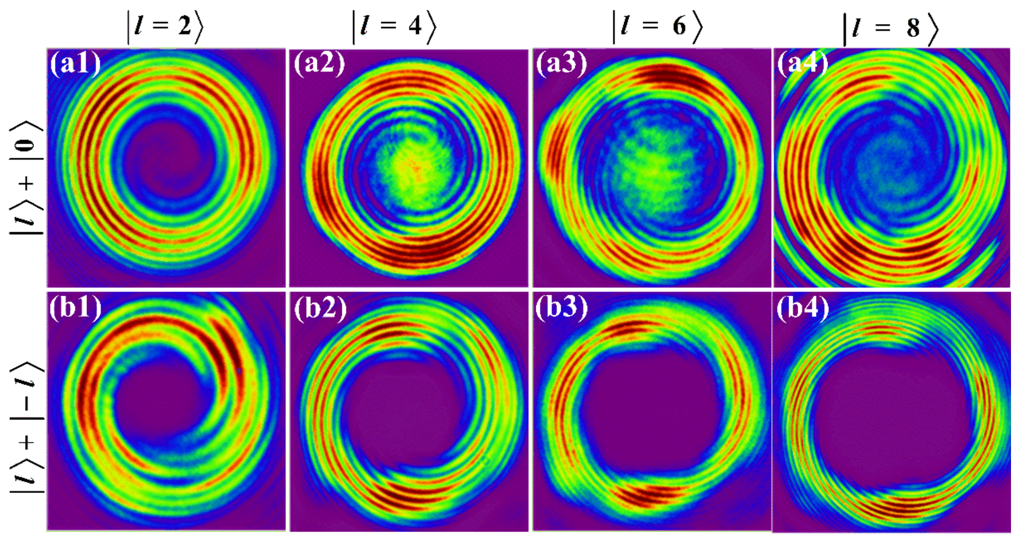

Figure 6. Coaxial interference patterns for two beams with different wavefront curvature radii. Images (**a1**–**a4**) are interference patterns between VB with TCs from 2 to 8 and a TEM_{00} Gaussian beam; Images (**b1**–**b4**) are interference patterns between VB with TCs from 2 to 8 and its conjugate one.

Similar to the above off-axis interference case, we also take the coaxial interference patterns between a VB with TCs 14 and a TEM_{00} Gaussian beam (its conjugate one) (shown in Figure 7) as an example for detailed introduction. For the coaxial interference pattern between VB and the spherical wave, the starting point of the helix is the location of the vortex (singularity). As shown in Figure 7a, there exist 14 starting points of helixes, and there is a counter-clockwise helix at each starting point. It demonstrates that the VB contains 14 single vortices with TC + 1 [61,62]. The locations of vortices are consistent with those shown in Figure 5a. The vortices numbers at certain region can also be determined by counting the helixes number. Lead out two auxiliary lines from the beam center, and make the other end of the line fall on the same helix. Count the number of helixes intersecting the two auxiliary lines, respectively. As shown in Figure 7a, the numbers of intersecting helixes are 5 on right side and 12 on the left side, respectively. Their difference (7) is just the vortex numbers between the two auxiliary lines. Figure 7b shows the coaxial interference patterns between VB with TCs of 14 and its conjugate one (the divergent beam). The number of counter-clockwise helixes is 28, which is just 2*l*.

For coaxial interference between two vortex beams with nearly the same wavefront curvature radii ($1/R_{l_1} \approx 1/R_{l_2}$) and bearing TCs of l_1 and l_2, petal patterns with $|l_1 - l_2|$ leaves are formed [49–51]. The experimental and simulated petal patterns are presented in Figure 8. Since the spot size of the generated VB is larger than that of the TEM_{00} Gaussian beam, the TEM_{00} Gaussian beam is expanded to be larger than the VB spot, and the interference pattern is measured at the position where the two interference spots overlap in space. Figure 8a1–a9 shows the experimental petal patterns with *l* leaves are formed by coaxial interference between a VB and a TEM_{00} Gaussian beam, respectively. The number of leaves in the petal patterns are just the TCs *l* carried by VB, and the beam center is not null. Figure 8a1,a2 show that the beam patterns encompass two and four equally spaced null regions, respectively. This is just the split of a highly charged vortex into individual unity-charged vortices reported in previous literature [26]. We also notice that the leaves of petal patterns rotate clockwise obviously for large *l* ($\geq$8). This is because the wavefront curvature radii of two interference beams satisfy: $1/R_{l_1} > 1/R_{l2}$, and the twist direction of the pattern is clockwise for $l_1 > l_2$ ($l > 0$). The petal patterns with slight twist can provide both the value and sign of TCs. Figure 8c1–c9 depicts the coaxial interference patterns between the VB and its conjugate one. The pattern with 2*l* bright petals, separated by 2*l* regions of dark petals, are generated. This is because two VBs have the same beam spot and wavefront curvature radius, they interfere constructively at 2*l* azimuthal positions, separated by 2*l* regions of destructive interference. To further verify the conclusion, we simulated the interference patterns using the theory shown in our previous work [47]. During the simulation process, the simulation parameters are carefully chosen to fit the experimental results. E.g., the phase difference of two interference beams is used to control the direction of the petals; the power ratio of two beams $P_2/P_1 = 0.1$; Suppose both beams have waist at $z = 0$, we choose $1 < w_2/w_1 < 2$ for the simulations shown in Figure 8b1–b9 and $w_2/w_1 = 1$ for the simulations shown in Figure 8d1–d9. The theoretical simulations show good consistency with the experimental ones.

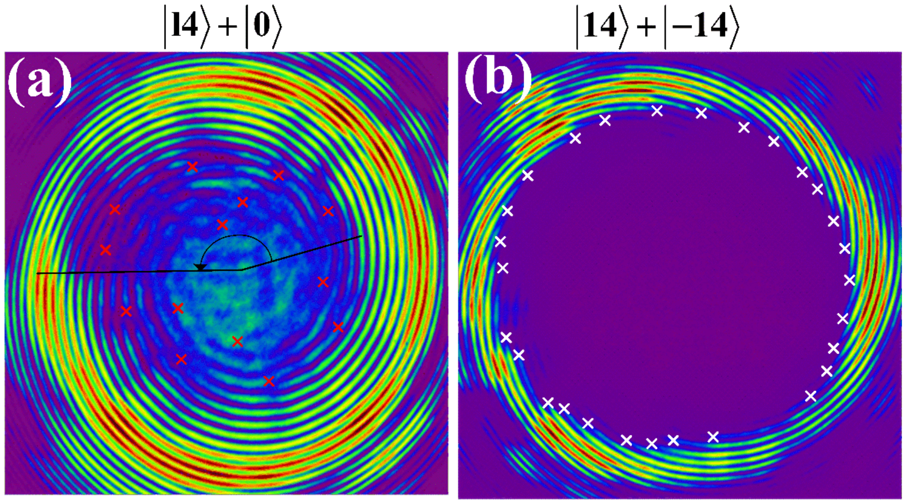

Figure 7. Coaxial interference patterns between two beams with different wavefront curvature radii. Image (**a**) is interference patterns between VB with TCs of 14 and a TEM_{00} Gaussian beam; image (**b**) is the interference patterns between VB with TCs of 14 and its conjugate one. The red crosses are used to denote the singularities' locations in image (**a**), and the white crosses denote the helixes.

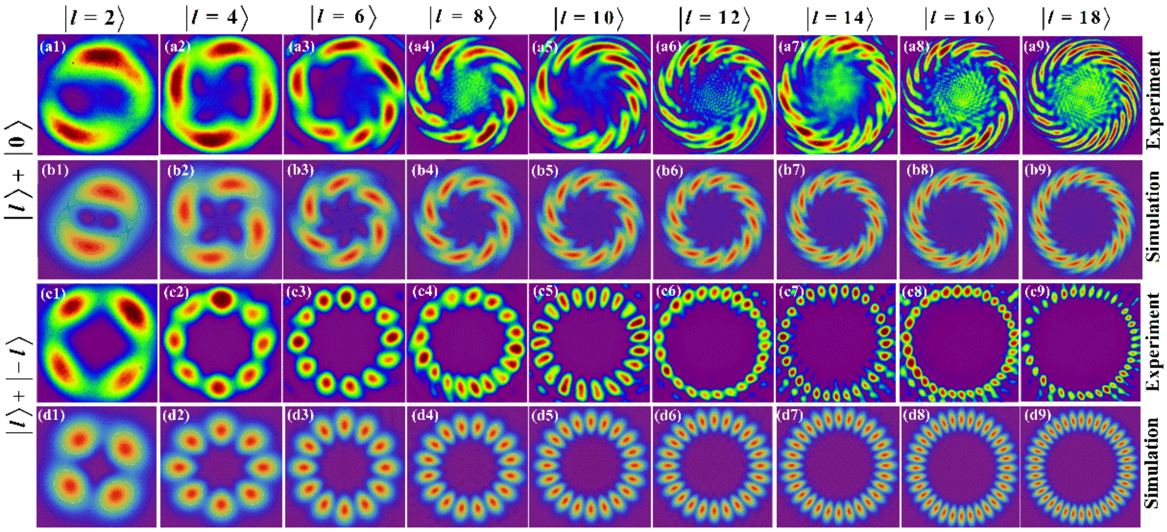

Figure 8. Coaxial interference patterns between two beams with nearly the same wavefront curvature radii. Images (**a1**–**a9**,**b1**–**b9**) are the interference patterns between VB and a TEM_{00} Gaussian beam theoretically and in experiment, respectively; Images (**c1**–**c9**,**d1**–**d9**) are the interference patterns between VB and its conjugate one theoretically and in experiment, respectively.

5. Conclusions

In summary, the VBs with even TCs from 2 to 18 are generated based on cascaded SPPs configuration. The typical doughnut-shaped intensity distribution for the VB illustrates that LG_{0l} mode dominates in the generated VB, even though the number of cascaded SPP is 6. The TCs can be increased (decreased) simply by the addition (subtraction) of SPPs. All these results indicate the cascaded SPPs configuration is reliable, practical, and effective. Besides, three kinds of interference patterns (fork, spiral and petal) about VBs are measured and compared about the competence on discriminating TCs. The fork, or spiral patterns allow us to distinguish the sign and value of TCs carried by the VB. The fork pattern shows better resolution than the spiral one, especially for large TCs, and the petal pattern with small spiral allows us to distinguish large TCs with a higher resolution.

Author Contributions: Conceptualization, Z.Z., P.L. and Y.G.; investigation, Z.Z. and P.L.; data curation, Z.Z. and P.L., writing—original draft preparation, Z.Z. and P.L.; theoretical calculation, Z.Z., S.Z. and P.L.; writing—review and editing, S.Z., J.M., P.L. and Y.G.; funding acquisition, P.L. and Y.G. All authors have read and agreed to the published version of the manuscript.

Funding: This work was supported by the Scientific and Technological Developing Scheme of Henan Province (202300410072), the Key Scientific Research Project of Colleges and Universities in Henan Province (18A140002), and the National Natural Science Foundation of China (NSFC) (61875053, 61805068, and 12104131).

Conflicts of Interest: The authors declare no conflict of interest.

References

1. Fürhapter, S.; Jesacher, A.; Bernet, S.; Ritsch-Marte, M. Spiral phase contrast imaging in microscopy. *Opt. Express* **2005**, *13*, 689–694. [CrossRef] [PubMed]
2. Plociniczak, L.; Popiolek-Masajada, A.; Szatkowski, M.; Masajada, M. High order vortex in the optical vortex microscope. *Proc. SPIE* **2015**, *9581*, 95810N.
3. Fickler, R.; Lapkiewicz, R.; Plick, W.N.; Krenn, M.; Schaeff, C.; Ramelow, S.; Zeilinger, A. Quantum Entanglement of High Angular Momenta. *Science* **2012**, *338*, 640–643. [CrossRef] [PubMed]
4. Fickle, R.; Campbell, G.; Buchler, B.; Lam, P.K.; Zeilinger, A. Quantum entanglement of angular momentum states with quan-tum numbers up to 10010. *Proc. Natl. Acad. Sci. USA* **2016**, *113*, 13642. [CrossRef] [PubMed]
5. Zhou, Z.Y.; Li, Y.; Ding, D.S.; Zhang, W.; Shi, S.; Shi, B.S. Optical vortex beam based optical fan for high-precision optical measurements and optical switching. *Opt. Lett.* **2014**, *39*, 5098–5101. [CrossRef] [PubMed]
6. Emile, O.; Emile, J. Naked eye picometer resolution in a Michelson interferometer using conjugated twisted beams. *Opt. Lett.* **2017**, *42*, 354–357. [CrossRef]
7. Wang, J.; Yang, J.Y.; Fazal, I.M.; Ahmed, N.; Yan, Y.; Huang, H.; Ren, Y.X.; Yue, Y.; Dolinar, S.; Tur, M.; et al. Terabit free-space data transmission employing orbital angular momentum multiplexing. *Nat. Photonics* **2012**, *6*, 488. [CrossRef]
8. Grier, D.G. A resolution in optical manipulation. *Nature* **2003**, *424*, 810. [CrossRef]
9. Allen, L.; Beijersbergen, M.W.; Spreeuw, R.J.C.; Woerdman, J.P. Orbital angular momentum of light and the transformation of Laguerre-Gaussian laser modes. *Phys. Rev. A* **1992**, *45*, 8185–8189. [CrossRef]
10. Forbes, K.A.; Andrews, D.L. Optical orbital angular momentum: Twisted light and chirality. *Opt. Lett.* **2018**, *43*, 435–438. [CrossRef]
11. Bai, Y.; Lv, H.; Fu, X.; Yang, Y. Vortex beam: Generation and detection of orbital angular momentum [Invited]. *Chin. Opt. Lett.* **2022**, *20*, 012601. [CrossRef]
12. Shen, Y.J.; Wang, X.J.; Xie, Z.W.; Min, C.J.; Fu, X.; Liu, Q.; Gong, M.L.; Yuan, X.C. Optical vortices 30 years on: OAM ma-nipulation from topological charge to multiple singularities. *Light Sci. Appl.* **2021**, *8*, 90. [CrossRef] [PubMed]
13. Chen, Y.; Fang, Z.X.; Ren, Y.X.; Gong, L.; Lu, R.D. Generation and characterization of a perfect vortex beam with a large top-ological charge through a digital micromirror device. *Appl. Opt.* **2015**, *54*, 8030–8035. [CrossRef] [PubMed]
14. Huang, K.; Liu, H.; Garcia-Vidal, F.J.; Hong, M.H.; Luk'yanchuk, B.; Teng, J.; Qiu, C.W. Ultrahigh-capacity non-periodic photon sieves operating in visible light. *Nat. Commun.* **2015**, *6*, 7059. [CrossRef]
15. Yang, Y.; Zhao, Q.; Liu, L.; Liu, Y.; Rosales-Guzmán, C.; Qiu, C.-W. Manipulation of Orbital-Angular-Momentum Spectrum Using Pinhole Plates. *Phys. Rev. Appl.* **2019**, *12*, 064007. [CrossRef]
16. Khonina, S.N.; Kotlyar, V.V.; Shinkaryev, M.V.; Soifer, V.A.; Uspleniev, G.V. The phase rotator filter. *J. Mod. Opt.* **1992**, *39*, 1147–1154. [CrossRef]
17. Beijersbergen, M.W.; Coerwinkel, R.P.C.; Kristensen, M.; Woerdman, J.P. Helical-wavefront laser beams produced with a spiral phaseplate. *Opt. Commun.* **1994**, *112*, 321–327. [CrossRef]
18. Turnbull, G.A.; Robertson, D.A.; Smith, G.M.; Allen, L.; Padgett, M.J. The generation of free-space Laguerre-Gaussian modes at millimetre-wave frequencies by use of a spiral phasplate. *Opt. Commun.* **1996**, *127*, 183–188. [CrossRef]
19. Machavariani, G.; Davidson, N.; Hasman, E.; Blit, S.; Ishaaya, A.A.; Friesem, A.A. Efficient conversion of a Gaussian beam to a high purity helical beam. *Opt. Commun.* **2002**, *209*, 265–271. [CrossRef]
20. Peele, A.G.; McMahon, P.J.; Paterson, D.; Tran, C.Q.; Mancuso, A.P.; Nugent, K.A.; Hayes, J.P.; Harvey, E.; Lai, B.; McNulty, I. Observation of an x-ray vortex. *Opt. Lett.* **2002**, *27*, 1752–1754. [CrossRef]
21. Sueda, K.; Miyaji, G.; Miyanaga, N.; Nakatsuka, M. Laguerre-Gaussian beam generated with a multilevel spiral phase plate for high intensity laser pulses. *Opt. Express* **2004**, *12*, 3548–3553. [CrossRef] [PubMed]
22. Watanabe, T.; Fujii, M.; Watanabe, Y.; Toyama, N.; Iketaki, Y. Generation of a doughnut-shaped beam using a spiral phase plate. *Rev. Sci. Instrum.* **2004**, *75*, 5131–5135. [CrossRef]
23. Rotschild, C.; Zommer, S.; Moed, S.; Hershcovitz, O.; Lipson, S.G. Adjustable spiral phase plate. *Appl. Opt.* **2004**, *43*, 2397–2399. [CrossRef] [PubMed]
24. Lee, W.M.S.; Yuan, X.-C.; Cheong, W.C. Optical vortex beam shaping by use of highly efficient irregular spiral phase plates for optical micromanipulation. *Opt. Lett.* **2004**, *29*, 1796–1798. [CrossRef] [PubMed]

25. Cheong, W.C.; Lee, W.M.; Yuan, X.-C.; Zhang, L.-S.; Dholakia, K.; Wang, H. Direct electron-beam writing of continuous spiral phase plates in negative resist with high power efficiency for optical manipulation. *Appl. Phys. Lett.* **2004**, *85*, 5784–5786. [CrossRef]
26. Moh, K.J.; Yuan, X.-C.; Cheong, W.C.; Zhang, L.S.; Lin, J.; Ahluwalia, B.P.S.; Wang, H. High-power efficient multiple optical vortices in a single beam generated by a kinoform-type spiral phase plate. *Appl. Opt.* **2006**, *45*, 1153–1161. [CrossRef]
27. Yuan, X.-C.; Lin, J.; Bu, J.; Burge, R.E. Achromatic design for the generation of optical vortices based on radial spiral phase plates. *Opt. Express* **2008**, *16*, 13599–13605. [CrossRef]
28. Wang, Q.; Sun, X.; Shum, P. Generating doughnut-shaped beams with large charge numbers by use of liquid-crystal spiral phase plates. *Appl. Opt.* **2004**, *43*, 2292–2297. [CrossRef]
29. Wang, Q.; Sun, X.W.; Shum, P.; Yin, X.J. Dynamic switching of optical vortices with dynamic gamma-correction liquid crystal spiral phase plate. *Opt. Express* **2005**, *13*, 10285–10291. [CrossRef]
30. Oemrawsingh, S.S.R.; Eliel, E.R.; Woerdman, J.P.; Verstegen, E.J.K.; Kloosterboer, J.G.; Hooft, G.W. Half-integral SPPs for op-tical wavelengths. *J. Opt. A Appl. Opt.* **2004**, *6*, S288–S290. [CrossRef]
31. Oemrawsingh, S.S.R.; van Houwelingen, A.W.; Eliel, E.R.; Woerdman, J.P.; Verstegen, E.J.K.; Kloosterboer, J.G.; 't Hooft, G.W. Production and characterization of spiral phase plates for optical wavelengths. *Appl. Opt.* **2004**, *43*, 688–694. [CrossRef] [PubMed]
32. Ruffato, G.; Massari, M.; Romanato, F. Generation of high-order Laguerre-Gaussian modes by means of spiral phase plates. *Opt. Lett.* **2014**, *39*, 5094–5097. [CrossRef] [PubMed]
33. Schemmel, P.; Pisano, G.; Maffei, B. A modular spiral phase plate design for orbital angular momentum generation at millimetre wavelengths. *Opt. Express* **2014**, *22*, 14712–14726. [CrossRef] [PubMed]
34. Shi, L.; Zhang, Z.; Cao, A.; Luo, X.; Deng, Q. One exposure processing to fabricate spiral phase plate with continuous surface. *Opt. Express* **2015**, *23*, 8620–8629. [CrossRef]
35. Massari, M.; Ruffato, G.; Gintoli, M.; Ricci, F.; Romanato, F. Fabrication and characterization of high-quality spiral phase plates for optical applications. *Appl. Opt.* **2015**, *54*, 4077–4083. [CrossRef]
36. Harm, W.; Bernet, S.; Ritsch-Marte, M.; Harder, I.; Lindlein, N. Adjustable diffractive spiral phase plates. *Opt. Express* **2015**, *23*, 413–421. [CrossRef]
37. Wu, W.-B.; Sheng, Z.-Q.; Wu, H.-W. Design and application of flat spiral phase plate. *Acta Phys. Sin.* **2019**, *68*, 054102. [CrossRef]
38. Isakov, D.; Wu, Y.; Allen, B.; Grant, P.S.; Stevens, C.J.; Gibbons, G.J. Evaluation of the Laguerre-Gaussian mode purity pro-duced by three-dimensional-printed microwave spiral phase plates. *R. Soc. Open Sci.* **2020**, *7*, 200493. [CrossRef]
39. Wei, Y. Propagation characteristic analysis of vortex beams produced by spiral phase plate. *Laser Infrared* **2016**, *46*, 857–861.
40. Wang, C.; Liu, T.; Ren, Y.; Shao, Q.; Dong, H. Generating optical vortex with large topological charges by spiral phase plates in cascaded and double-pass configuration. *Optik* **2018**, *171*, 404–412. [CrossRef]
41. Ren, Y.; Wang, C.; Liu, T.; Shao, Q. Method of optical vortex generation by cascaded spiral phase plates. In Proceedings of the Optical Precision Manufacturing, Testing, and Applications, Beijing, China, 12 December 2018; SPIE: Bellingham, WA, USA, 2018; Volume 10847, p. 1084703. [CrossRef]
42. Wang, C.; Liu, T.; Shao, Q.L.; Ren, Y.; Miao, J.S. Quadrupling topological charges of vortex using multi-passed spiral phase plate. *Infrared Laser Eng.* **2018**, *47*, 0918008. [CrossRef]
43. Ma, J.; Li, P.; Zhou, Z.; Gu, Y. Characteristics of fork-shaped fringes formed by off-axis interference of two vortex beams. *J. Opt. Soc. Am. A* **2020**, *38*, 115–123. [CrossRef] [PubMed]
44. Kumar, P.; Nishcal, N.K. Modified Mach-Zehnder interferometer for determining the high-order topological charge of La-guerre-Gaussian vortex beam. *J. Opt. Soc. Am. A* **2019**, *36*, 1447–1455. [CrossRef] [PubMed]
45. Bazhenov, V.Y.; Vasnetsov, M.V.; Soskin, M.S. Screw dislocations of wavefront. *J. Mod. Opt.* **1992**, *39*, 985–990. [CrossRef]
46. Wang, J.; Cao, A.; Zhang, M.; Pang, H.; Hu, S.; Fu, Y.; Shi, L.; Deng, Q. Study of Characteristics of Vortex Beam Produced by Fabricated Spiral Phase Plates. *IEEE Photonics J.* **2016**, *8*, 1–9. [CrossRef]
47. Ma, J.B.; Li, P.; Gu, Y.Z. Characteristics of spiral patterns formed by coaxial interference between two vortex beams with dif-ferent radii of wavefront curvatures. *Photonics* **2021**, *8*, 393. [CrossRef]
48. Cui, S.; Xu, B.; Luo, S.; Xu, H.; Cai, Z.; Luo, Z.; Pu, J.; Chávez-Cerda, S. Determining topological charge based on an improved Fizeau interferometer. *Opt. Express* **2019**, *27*, 12774–12779. [CrossRef]
49. Pan, S.; Pei, C.; Liu, S.; Wei, J.; Wu, D.; Liu, Z.; Yin, Y.; Xia, Y.; Yin, J. Measuring orbital angular momentums of light based on petal interference patterns. *OSA Contin.* **2018**, *1*, 451–461. [CrossRef]
50. Galvez, E.J.; Smiley, N.; Fernandes, N. Composite optical vortices formed by collinear Laguerre-Gauss beams. In Proceedings of the Nanomanipulation with Light II, San Jose, CA, USA, 9 February 2006; SPIE: Bellingham, WA, USA, 2006; Volume 131, p. 613105. [CrossRef]
51. Lv, F.; Li, X.; Tai, Y.; Zhang, L.; Nie, Z.; Chen, Q. High-order topological charges measurement of LG vortex beams with a modified Mach–Zehnder interferometer. *Optik* **2015**, *126*, 4378–4381. [CrossRef]
52. Zhang, Y.; Li, P.; Zhong, J.; Qi, S.; Guo, X.; Wu, D.; Liu, S.; Zhao, J. Measuring singularities of cylindrically structured light beams using a radial grating. *Appl. Phys. Lett.* **2018**, *113*, 221108. [CrossRef]
53. Zhao, Q.; Dong, M.; Bai, Y.; Yang, Y. Measuring high orbital angular momentum of vortex beams with an improved multipoint interferometer. *Photon. Res.* **2020**, *8*, 745. [CrossRef]

54. Narag, J.P.C.; Hermosa, N. Probing Higher Orbital Angular Momentum of Laguerre-Gaussian Beams via Diffraction through a Translated Single Slit. *Phys. Rev. Appl.* **2019**, *11*, 054025. [CrossRef]
55. Li, C.; Zhao, S. Efficient separating orbital angular momentum mode with radial varying phase. *Photon. Res.* **2017**, *5*, 267–270. [CrossRef]
56. Wen, Y.; Chremmos, I.; Chen, Y.; Zhu, J.; Zhang, Y.; Yu, S. Spiral Transformation for High-Resolution and Efficient Sorting of Optical Vortex Modes. *Phys. Rev. Lett.* **2018**, *120*, 193904. [CrossRef] [PubMed]
57. Zhou, J.; Zhang, W.; Chen, L. Experimental detection of high-order or fractional orbital angular momentum of light based on a robust mode converter. *Appl. Phys. Lett.* **2016**, *108*, 111108. [CrossRef]
58. Kotlyar, V.V.; Elfstrom, H.; Turunen, J.; Almazov, A.A.; Khonina, S.; Soifer, V. Generation of phase singularity through diffracting a plane or Gaussian beam by a spiral phase plate. *J. Opt. Soc. Am. A* **2005**, *22*, 849–861. [CrossRef]
59. Mawardi, A.; Hild, S.; Widera, A.; Meschede, D. ABCD-treatment of a propagating doughnut beam generated by a spiral phase plate. *Opt. Express* **2011**, *19*, 21205–21210. [CrossRef]
60. Gradshteyn, I.S.; Ryzhik, I.M. *Table of Integrals, Series and Products*; Academic Press: New York, NY, USA, 2007.
61. Soskin, M.S.; Gorshkov, V.N.; Vasnetsov, M.V.; Malos, J.T.; Heckenberg, N.R. Topological charge and angular momentum of light beams carrying optical vortices. *Phys. Rev. A* **1997**, *56*, 4064–4075. [CrossRef]
62. Mao, B.; Liu, Y.; Chang, W.; Chen, L.; Feng, M.; Guo, H.; He, J.; Wang, Z. Singularities splitting phenomenon for the superposition of hybrid orders structured lights and the corresponding interference discrimination method. *Nanophotonics* **2022**, *11*, 1413–1426. [CrossRef]